Research Article

Hanjing Zhu, Baohong Tian*, Yi Zhang*, Meng Zhou*, Yunzhang Li, Xianhua Zheng, Shengli Liang, Shuang Liu, Wenyu Sun, Yong Liu, and Alex A. Volinsky

Microstructure and electrical contact behavior of the nano-yttria-modified Cu-Al_2O_3/30Mo/3SiC composite

https://doi.org/10.1515/ntrev-2022-0532
received October 3, 2022; accepted March 8, 2023

Abstract: With the rapid development of the copper-based composite in the field of electrical contact material industry, the problem of poor arc erosion resistance of the copper-based material becomes more and more prominent. Improving the arc erosion resistance of the copper-based composite is an urgent problem to be solved. Cu-Al_2O_3/30Mo/3SiC and 0.5Y_2O_3/Cu-Al_2O_3/30Mo/3SiC electrical contact composites were prepared in a fast-hot-pressing sintering furnace. The microstructure and phase structure of the composites were analyzed by using a scanning electron microscope, transmission electron microscope, and X-ray diffraction meter, respectively. The arc erosion properties of the composites at 25 V, DC and 10-30 A were investigated by using a JF04C electric contact tester. The mass loss of the composites was reduced by 77.8%, and the arc erosion rate was reduced by 79.6% after the addition of nano-yttrium oxide under the experimental conditions of 25 V, DC and 30 A. At the same time, the arc energy and welding force of the composite after switching operations decreased, indicating that the addition of nano-yttria improved the arc erosion resistance of the composite. This work provides a new method for improving the arc erosion resistance of the copper-based composite contact material.

Keywords: copper-based composite, nano-alumina particles, electrical contact, nano-yttria, 0.5Y_2O_3/Cu-Al_2O_3/30Mo/3SiC

*** Corresponding author: Baohong Tian,** School of Materials Science and Engineering, Henan University of Science and Technology, Luoyang 471023, China; Provincial and Ministerial Co-construction of Collaborative Innovation Center for Non-ferrous Metal New Materials and Advanced Processing Technology, Luoyang, 471023, China; Henan Key Laboratory of Nonferrous Materials Science and Processing Technology, Luoyang 471023, China,
e-mail: bhtian007@163.com
*** Corresponding author: Yi Zhang,** School of Materials Science and Engineering, Henan University of Science and Technology, Luoyang 471023, China; Provincial and Ministerial Co-construction of Collaborative Innovation Center for Non-ferrous Metal New Materials and Advanced Processing Technology, Luoyang, 471023, China; Henan Key Laboratory of Nonferrous Materials Science and Processing Technology, Luoyang 471023, China,
e-mail: zhshgu436@163.com
*** Corresponding author: Meng Zhou,** School of Materials Science and Engineering, Henan University of Science and Technology, Luoyang 471023, China; Provincial and Ministerial Co-construction of Collaborative Innovation Center for Non-ferrous Metal New Materials and Advanced Processing Technology, Luoyang, 471023, China; Henan Key Laboratory of Nonferrous Materials Science and Processing Technology, Luoyang 471023, China,
e-mail: zhoumeng0902@126.com
Hanjing Zhu, Yunzhang Li, Xianhua Zheng, Shengli Liang, Shuang Liu, Wenyu Sun, Yong Liu: School of Materials Science and Engineering, Henan University of Science and Technology, Luoyang 471023, China; Provincial and Ministerial Co-construction of Collaborative Innovation Center for Non-ferrous Metal New Materials and Advanced Processing Technology, Luoyang, 471023, China; Henan Key Laboratory of Nonferrous Materials Science and Processing Technology, Luoyang 471023, China
Alex A. Volinsky: Department of Mechanical Engineering, University of South Florida, 4202 E. Fowler Ave. ENG030, Tampa 33620, United States of America

1 Introduction

With the rapid development of the power industry, ultra-high-voltage, large capacity, and long-distance power transmission have gradually become the trend of energy-saving power transmission [1,2]. Vacuum high-voltage switchgear plays an important role in high-voltage power transmission apparatus and equipment [3,4]. Vacuum high-voltage switches are also called vacuum circuit breakers, and the key component is their contact material [5]. The performance of electrical contact materials directly affects the technical level of power generation, transmission, and transformation equipment [6]. Electrical contact refers to the physical and chemical phenomena in which two conductors contact each other and transmit current or signals

through the contact interface [7]. Due to the limitation of its working environment, the contact material should have some basic characteristics: excellent electrical conductivity and thermal conductivity [8,9], low contact resistance and high temperature [10], excellent breaking ability [11], resistance to welding and environmental media pollution [12], and good physical and mechanical processing performance [13]. The traditional electrical contact material is silver-based composites, which have a high cost [14,15]. Therefore, all countries are committed to developing a variety of new electrical contact materials to meet the requirements.

Copper-based composite for electrical contact use appears in the public eye [16,17]. Copper (Cu) has excellent electrical conductivity and thermal conductivity. In recent years, with the rapid development of copper-based composite, the copper–tungsten (Cu–W) series, copper–molybdenum (Cu–Mo) series, and copper–chromium (Cu–Cr) series as the mainstream have been gradually developed [18]. Molybdenum (Mo) has the characteristics of a high melting point and high hardness. Molybdenum can form an "artificial alloy" with copper. The Cu–Mo series composite is mainly used in vacuum switch tubes [19]. Biyik milled the powder containing 25 wt% Mo in a high-energy planetary-type ball mill to achieve homogeneously mixed Cu25Mo composite powder [20]. The nanocrystalline powder was obtained after ball milling for 30 h, which is helpful to improve the properties of composites. Alumina diffusion-reinforced copper (Cu-Al_2O_3) can greatly improve the strength of the substrate. The introduction of diffusely distributed alumina particles into the copper matrix can impede dislocation movement and inhibit recrystallization [21]. Cu-Al_2O_3 prepared by the internal oxidation process is widely used in electrical contact materials. For example, Wang *et al.* [22] investigated the effect of alumina particles on the deformation behavior of copper-based materials by the nano-indentation method. It was found that the displacement recovery ratio and elastic work ratio are 6 and 9% higher for the 5 wt% Cu-Al_2O_3 composite compared with the pure copper material, respectively. Hussain *et al.* [23] prepared the Cu-Al_2O_3 composite with different contents (0, 1%, 3%, and 5%) of alumina by the powder metallurgy method. It was found that with the increase of alumina content, the relative density, micro-hardness, friction, and wear resistance of the composites were significantly improved. Wagih *et al.* [24] prepared Cu-Al_2O_3/graphene nanoplatelets (GNPs) coated silver nanocomposite with different GNP contents. The compressive strength and hardness of the composite increase by 88.1 and 55.2% with the increase of the GNP content, respectively. Silicon carbide (SiC) is the second particle of copper-based composite and it has great potential in the field of advanced electronic packaging material. The electric conductivity of the silicon carbide-reinforced copper-based composite does not decrease while the strength and high-temperature strength are improved. Akbarpour *et al.* [25] investigated the influence of the silicon carbide content on the microstructure, mechanical, and magnetic properties of the $Cu_{(1-x)}SiC$ (x = 0, 2, 10, and 15 wt%) composite powder. It was found that when the silicon carbide content is 15 wt%, the Vickers micro-hardness reaches a maximum value of 135.22 HV. Dong *et al.* [26] prepared the 15 vol% SiC_{nw}/6061Al composite by the pressure infiltration method and found that this composite demonstrates high strength (over 1,000 MPa). Feng *et al.* [27] investigated the effect of SiC addition on the Al_2O_3/Cu composites and found that a small amount of SiC addition can improve the strength of the composites. At the same time, relevant studies have shown that the addition of some secondary additives (*e.g.*, nano-yttria (Y_2O_3), boric oxide (B_2O_3), and cerium oxide (CeO_2)) can limit the negative arc effect and prolong the contact life of electrical contact materials [28–30].

Rare earth metals have the ability to promote recrystallization, refine grains, strengthen the matrix, and possess high melting points and good stability [31,32]. Liu *et al.* [33] added Ce_2O and graphene oxide (GO) to the copper–chromium (Cu–Cr) composite to prepare the GO-Cu/0.5Ce_2O30Cr composite. The composite showed excellent electrical contact properties and anti-fusion welding properties. Liang *et al.* [34] introduced GO and Ce_2O into the Cu30Cr10W composite contact material with excellent mechanical properties and welding resistance. As a typical rare earth metal oxide, nano-yttria has attracted extensive attention in recent years [35,36]. Nano-yttria is an ideal reinforcing phase for copper-based composite with excellent thermodynamic stability, wettability, and chemical stability [37–39]. Huang *et al.* [40] prepared the Cu–10 vol% Y_2O_3 nanocomposite by the traditional mechanical alloying (MA) method. The micro-hardness of the Cu–10 vol% Y_2O_3 nanocomposite reached 209.6 HV, with a compressive strength of 655 MPa and a plasticity of 33.4%. Huang *et al.* [41] found that the addition of yttrium oxide to the copper-based composite can refine its grain. At the same time, with the increase of the Y_2O_3 content, the relative density and Vickers hardness of the composite increased. Y_2O_3 shows an excellent reinforcing effect in copper-based electrical contact material. Mu *et al.* [42] found that the arc erosion resistance of composites was significantly improved after the addition of Y_2O_3. The contact resistances of the composite still kept a lower value after 20,000 switching operations.

At present, the commonly used methods for preparing particle-reinforced composites include the external forcing

method and the internal autogenous method. The external strengthening method includes the powder metallurgy method [43] and MA [44]. The internal autogenetic method includes the *in situ* autogenetic method [45], internal oxidation method [46], and chemical coating on the particle surface [47]. The composite can show the best comprehensive performance by formulating the preparation process [48]. In the process of preparing composites by powder metallurgy, in order to improve the compactness and sintering shrinkage of mixed powder and to increase the density of composites, more liquid phase sintering components can be added to the alloy. The commonly used reinforcement is SiC [49,50], titanium carbide (TiC) [51], and boron nitride (BN) [52].

The above research status and the previous research work of our group [17] showed that the composites with the addition of 30 wt% refractory metals have more excellent comprehensive properties. The addition of a small amount of SiC can improve the performance of electrical contact materials without sacrificing the physical properties [27]. The addition of a small amount of Y_2O_3 can reduce the contact resistance of electrical contacts and exhibit superior electrical contact performance [42]. In this work, Cu-Al_2O_3/30Mo/3SiC and 0.5Y_2O_3/Cu-Al_2O_3/30Mo/3SiC composites were prepared by powder metallurgy and internal oxidation methods. The relative density, electrical conductivity, and Vickers hardness were measured. The microstructure and electrical contact properties, including the mass transfer, arc duration, arc time, and welding force, of the two composites were investigated, respectively.

2 Experimental details

2.1 Composite fabrication

The feedstock of the composite included the copper–0.2 wt% aluminum (Cu–0.2% Al) alloy powder with an average particle size of 37 μm, cuprous oxide (Cu_2O) powder of 2–5 μm, molybdenum powder of 5–8 μm, silicon carbide powder of 3–5 μm, and nano-yttria powder of 50 nm. These powders were commercially available. The chemical composition of the Cu–0.2% Al alloy powder is shown in Table 1. The contents of trace impurity elements, iron (Fe), aluminum (Al), zinc (Zn), tin (Sn), lead (Pb), and nickel (Ni) in the –0.2% Al alloy powder were determined by inductively coupled plasma-atomic emission spectroscopy (ICP-AES). Table 2 shows the specific component content of the Cu-Al_2O_3/30Mo/3SiC and 0.5Y_2O_3/Cu-Al_2O_3/30Mo/3SiC composites; 30Mo represents 30 wt% Mo, 3SiC represents 3 wt% SiC, 0.5Y_2O_3 represents 0.5 wt% Y_2O_3, and the rest for Cu-Al_2O_3. The fabrication processing routine of the two composites is as follows (Figure 1). The Cu–0.2% Al alloy powders, cuprous oxide, molybdenum, silicon carbide, and nano-yttria powders with different mass percentages were put into a self-made ball grinding tank. The composite powders were ball milled. A traditional QQM/B light ball mill was used in the process of ball milling. The test parameters were set as follows: continuous ball milling for 4 h, rotating speed of 50 rpm, and the ratio of composite powders and copper balls was 1:3. No coolant was used during ball milling to maintain the original morphology of the powders. A certain amount of composite powders after ball milling was weighed and placed in a graphite grinding tool. A layer of graphite paper was wrapped in the inner ring of the graphite abrasive in order to avoid powders sticking on the graphite wall. The graphite grinding tool was sintered in a fast hot press sintering furnace (FHP-828). The vacuum degree in the furnace was controlled below 10 Pa, the sintering pressure was 45 MPa, and the heating rate was 100°C/min. The sintering process was divided into three stages: the sintering temperature was set to 700°C, held for 10 min, and then continued to heat up to 950°C and held for 10 min; finally the composite was took out when the temperature in the furnace cooled to 100°C.

Table 2: Composition of copper-based composites (wt%)

Composites	Cu-0.2% Al	Mo	SiC	Cu_2O	Y_2O_3
Cu-Al_2O_3/30Mo/3SiC	65.2	30	3	1.8	/
0.5Y_2O_3/Cu-Al_2O_3/30Mo/3SiC	64.7	30	3	1.8	0.5

Table 1: Chemical composition of the Cu–0.2% Al alloy powder (wt%)

Elements	Fe	Al	Zn	Sn	Pb	Ni
Mass percent	0.004522	0.242343	0.000536	0.021612	0.000776	0.00117

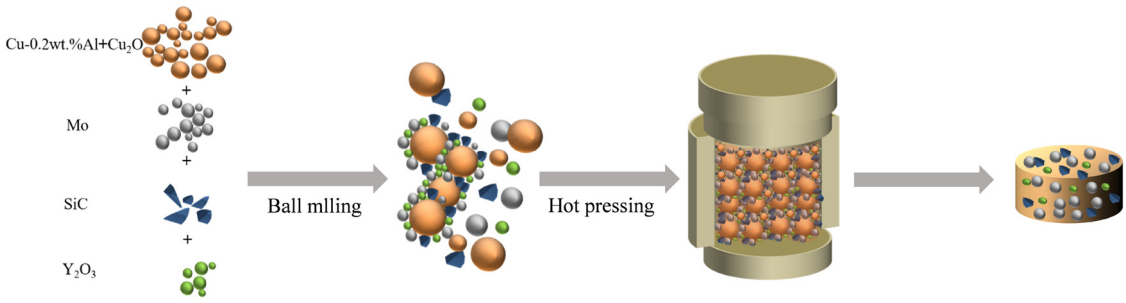

Figure 1: Schematic illustration of the preparation process of Cu-Al_2O_3/30Mo/3SiC and 0.5Y_2O_3/Cu-Al_2O_3/30Mo/3SiC composites.

2.2 Mechanical and physical properties

In order to avoid the influence of surface and roughness on the basic properties, the sintered composite ingots were polished with sandpaper of different grit sizes and then mechanically polished with W 0.5 diamond abrasive paste. The following basic properties tests were performed on the composites after the above operations. Eight measurements were taken for each composite ingot using a Sigma 2008 B1 digital conductivity meter and the average was taken. The actual density of the composites was determined with a hydrostatic balance (MS105) using deionized water under 21°C as the liquid medium. The relative density of the composites was calculated according to the principle of Archimedes' drainage method. The Vickers hardness of the composites was measured with an HV-1000 microhardness tester, and each composite was measured eight times and averaged. The test force was 50 g with a loading time of 10 s.

2.3 Microstructure characterization

The original powder, composite powder, and microscopic morphology after arc erosion were observed under a scanning electron microscope (SEM, JSM-IT100). The signal source of the SEM was a secondary electron with an acceleration voltage of 20 kV, a working distance of 11 mm, and a probing current of 50 nA. The composite samples used in SEM were polished to 2,000 mesh with sandpaper. Mirror polishing was carried out with the W 0.5 diamond scrub cream.

The surface morphology of sintered and arc erosion composites was observed under a field emission scanning electron microscope (FESEM, JEOL JSM-7800F). The elemental distribution on the surface of the composites after sintering and arc erosion was analyzed by energy dispersive X-ray spectrometer (EDS, 20 mm^2 X-Max^N Silicon Drift Detector) with a FESEM. FESEM was performed with accelerating voltages ranging from 0.01 to 30 kV and a probing current of 200 nA (15 kV).

The crystal structure of the composite powder and sintered composites were analyzed by X-ray diffraction (XRD, D8 advanced X). XRD tests were performed using copper Kα radiation, operating at 40 kV and 40 mA, with a step size of 0.2° and a scan range (2θ) of 30–92°.

The dislocation structure and microstructure of different phases were characterized by transmission electron microscopy (TEM, FEI Talos F200X). The microscope used worked below 200 kV. The composite samples used for TEM with 500 μm in thickness sheets need to be manually polished to about 100 μm and then ion thinning. Ion thinning was performed on a Gatan 695 ion thinning instrument. A starting voltage of 5 keV and an ion gun angle of ±8° were used for trenching and initial thinning, and the electron gun angle was reduced to 4.5 keV ±6° for 5 min of thinning, 4 keV ±4° for 5 min of thinning, and 5 min of thinning at 3 keV ±3° to obtain TEM samples.

2.4 Arc-erosion tests

Cylindrical composite samples with 3.8 mm in diameter and 10 mm in height were used as the anode and cathode of the electrical contact test. To ensure the accuracy of the experimental data, the samples were manually polished and mechanically polished with a W 0.5 diamond scrub cream before the test. The masses of the composites before and after electrical contact were weighed with an electronic balance (FA2004B), and each composite was weighed five times to obtain the average value. The change in the mass of the composites before and after the electrical contact test was expressed as Δm as follows:

$$\Delta m = m_e - m_b, \tag{1}$$

where m_e represents the composite mass after the switching operations and m_b represents the composite mass before the switching operations.

The arc erosion experiment was carried out after 5,000 switching operations on a JF04C electrical contact experimental device. The moving contact was the anode and the static contact was the cathode. The test voltage was 25 V, DC, and the currents were 10, 20, 25, and 30 A, respectively. The contact force was maintained between 40 and 60 cN.

The model three-dimensional (3-D) morphology of the cathode and anode after the electric contact experiment was characterized by a nano focusing 3-D topography instrument.

3 Results

3.1 Microstructure

The original powder morphology of Cu–0.2% Al, molybdenum, silicon carbide, and cuprous oxide are shown in Figure 2. It was found that the Cu–0.2% Al alloy particles, molybdenum particles, and cuprous oxide particles were generally spherical, while the morphology of silicon carbide particles had irregular sharp shapes with a wide range of size. The morphology of Cu-Al_2O_3/30Mo/3SiC and 0.5Y_2O_3/Cu-Al_2O_3/30Mo/3SiC composite powders after ball milling are shown in Figure 2(e) and (f). It can be found that the different particles in the composite powder were uniformly distributed when the ball/material ratio during the ball milling process was 3:1. The morphology of the various powders did not change significantly before and after ball milling. The spherical shape of the particles can ensure that the composites maintain better flowability during the sintering process, which is conducive to improving the relative density of the composites.

The XRD analysis results of Cu-Al_2O_3/30Mo/3SiC and 0.5Y_2O_3/Cu-Al_2O_3/30Mo/3SiC powders and as sintered composites are shown in Figure 3. From Figure 3(a) and (b), it can be seen that the (111), (200), (220), (311) diffraction peaks of the copper matrix are higher than the (110), (200), (211), (220) diffraction peaks of the main strengthening phase molybdenum, irrespective of the composite powder before sintering or the compact body after sintering, although molybdenum also has a higher diffraction peak. Interestingly, it is found that small diffraction peaks have changed between 35° and 40° as shown in Figure 3(c) and (d). The results indicate that the reaction of Cu_2O is complete after sintering. Other particles are not shown in the XRD spectrum as small amounts were added.

Figure 4 shows the microstructures and EDS results of sintered Cu-Al_2O_3/30Mo/3SiC and 0.5Y_2O_3/Cu-Al_2O_3/30Mo/3SiC composites, respectively. Molybdenum particles, silicon carbide particles, and nano-yttria particles were evenly distributed on the copper base without obvious agglomeration, pores, and other defects, as shown in Figure 4(a)–(d). From the line scanning EDS results of molybdenum particles and silicon carbide particles, the copper base was closely combined with the main reinforcing particles, as shown in Figure 4(f) and (g). Figure 4(e) and (h) shows the EDS data of Cu-Al_2O_3/30Mo/3SiC and 0.5Y_2O_3/Cu-Al_2O_3/30Mo/3SiC composites.

Figure 5 shows the TEM, HRTEM images, and EDS point sweep data of the 0.5Y_2O_3/Cu-Al_2O_3/30Mo/3SiC

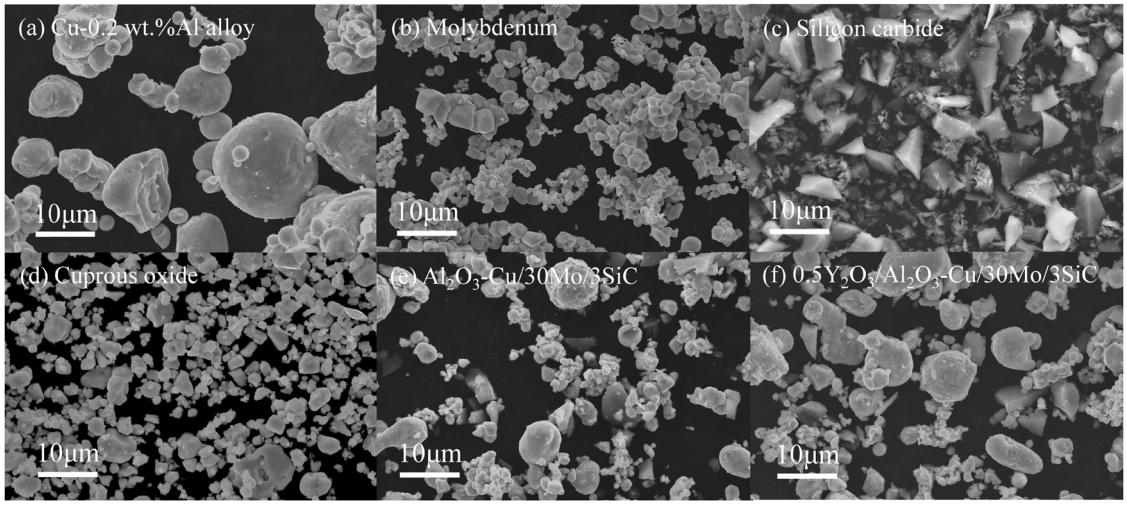

Figure 2: SEM images of feedstock and composite powders: (a) Cu-0.2% Al alloy, (b) molybdenum, (c) silicon carbide, (d) cuprous oxide, (e) Cu-Al_2O_3/30Mo/3SiC composite, and (f) 0.5Y_2O_3/Cu-Al_2O_3/30Mo/3SiC composite.

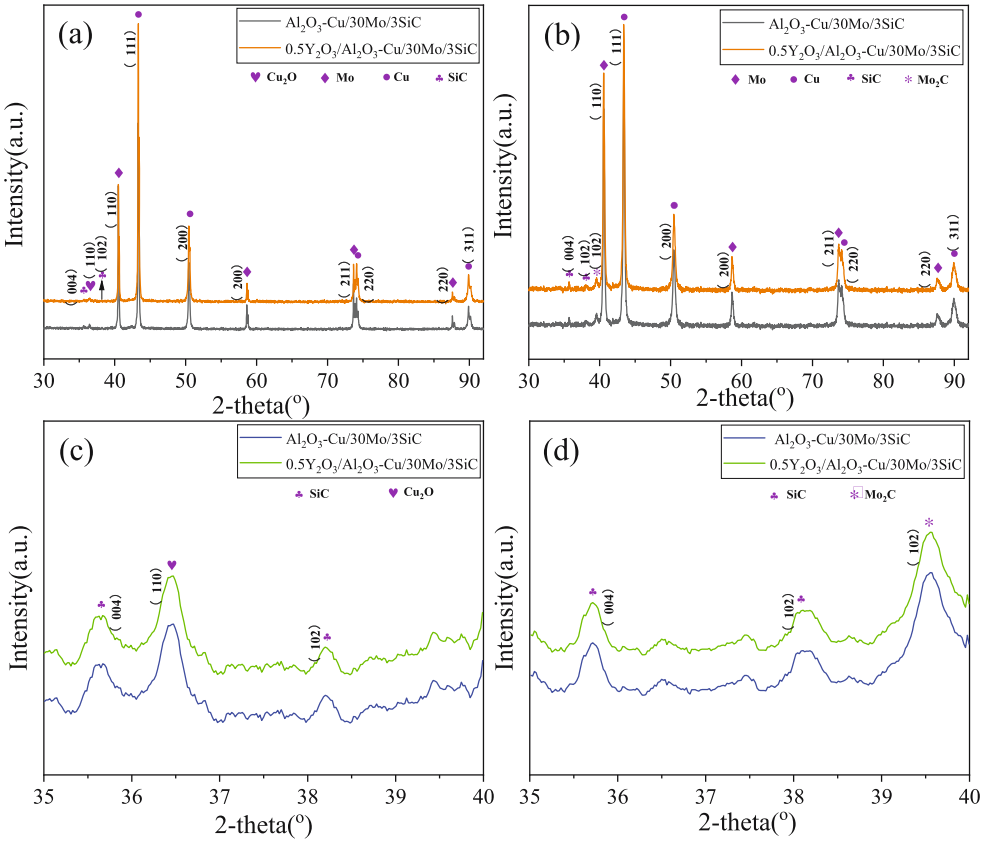

Figure 3: XRD spectrum of Cu-Al_2O_3/30Mo/3SiC and 0.5Y_2O_3/Cu-Al_2O_3/30Mo/3SiC powders and as sintered composites. (a and c) XRD spectrum of composite powders as milled and (b and d) XRD spectrum of composites as sintered.

composite. A large number of alumina nanoparticles were formed *in situ* in the composite and evenly distributed on the copper matrix, as shown in Figure 5(a) and (g). Figure 5(b) shows the HRTEM image of the part area of Figure 5(a). Figure 5(c)–(e) shows the point scan data of the corresponding areas in Figure 5(a) and (b); so it is evident that area A_1 is of the MoC particle, area B_1 is of the copper base, and area C_1 is of the silicon carbide particle. The formation of the hard-phase MoC particles facilitates the improvement of the mechanical properties of composites. In Figure 5(f), it can be determined by fast Fourier transform that the internal oxidation process generated γ-alumina. In Figure 5(g), alumina nanoparticles are dispersed on the copper base, pinning dislocations and causing dislocation tangling. The size of these alumina particles is about 5–20 nm and the spacing is about 25–60 nm. Nano-dispersed particles and spacing can act as a source of dislocations and increase the dislocation density of the substrate during cold deformation, which hinders the dislocation and grain boundary motion. When a large number of nanoparticles are dispersed on the copper matrix, they will nail dislocations and form dislocation stacking and high-density dislocations. The high-density dislocations are interwoven to further form dislocation units, thus acting as dispersion reinforcement and improving the high-temperature performance of the contact. Figure 5(h) shows some high-density dislocations and dislocation cells.

3.2 Mechanical and physical properties

The relative density, electrical conductivity, and microhardness of the two composites are shown in Table 3. The relative density of the Cu-Al_2O_3/30Mo/3SiC composite was only 97.14% before the addition of nano-yttria, and the relative density of 0.5Y_2O_3/Cu-Al_2O_3/30Mo/3SiC composite could reach more than 98% after the addition of nano-yttria. Spherical nanoparticles of nano-yttria have good mobility, and can be evenly distributed in the copper matrix [53]. In the sintering process of the composite material, the pores generated by the accumulation of matrix particles can be filled. The relative density of composites is increased. Compared with the composites without nano-yttria, the electrical conductivity of the composites with nano-yttria is improved. This is mainly because the electrons are less hindered from moving

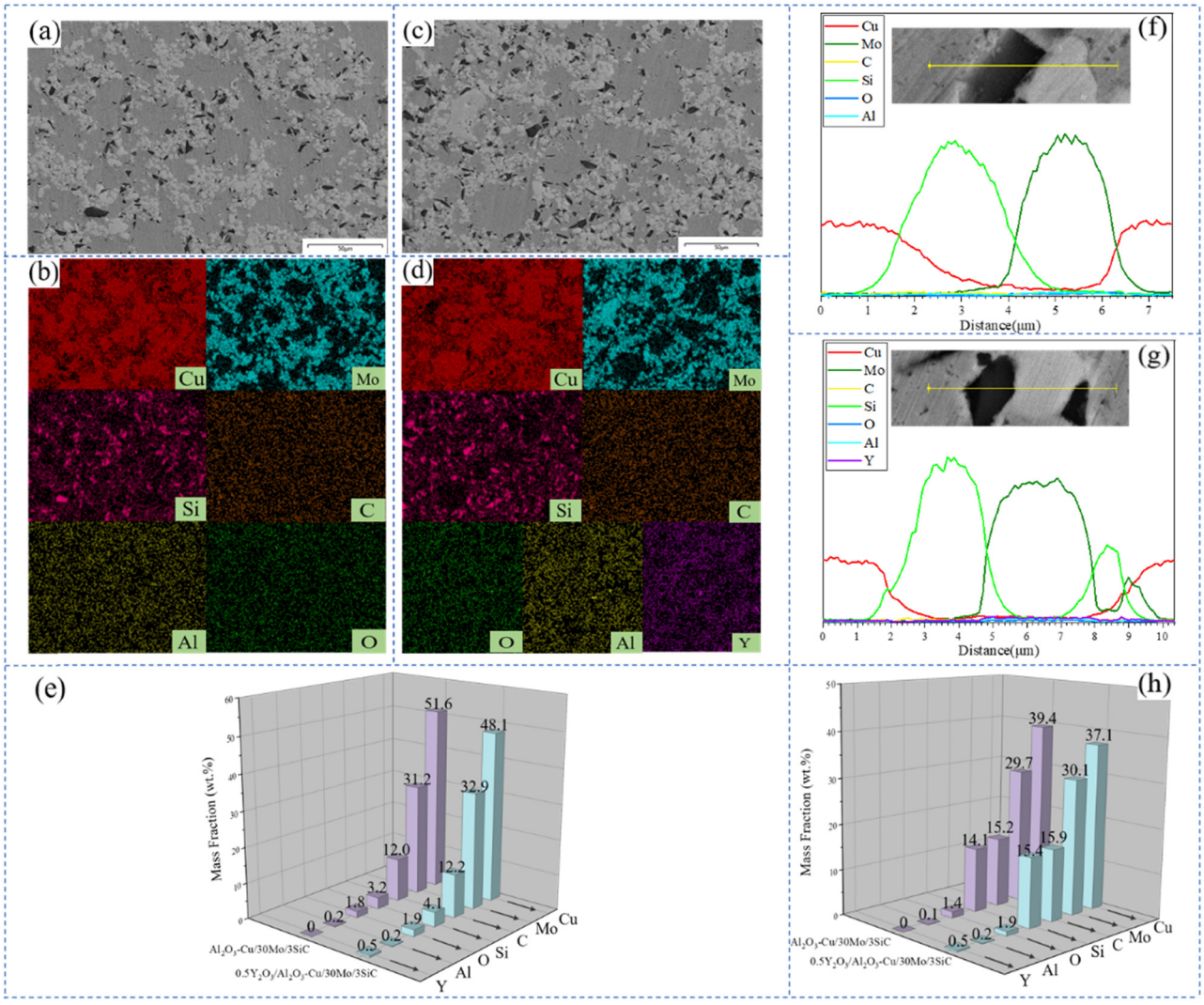

Figure 4: SEM images and EDS maps of as-sintered composites. (a, b, f) Cu-Al_2O_3/30Mo/3SiC composite, (c, d, g) 0.5Y_2O_3/Cu-Al_2O_3/30Mo/3SiC composite, (e) EDS map data of two composites, and (h) EDS lines data of the two composites.

while there are fewer pores in the composite material while moving. When the scattering of electrons by pores decreases, the resistance inside the composite decreases and the conductivity increases. Nano-yttria has good thermal stability and does not grow during the sintering process [54]. Meanwhile, nano-yttria can inhibit the growth of copper grains since it is often distributed around grain boundaries. Thus, it acts as a fine-grained reinforcement [55]. These factors promote the increase of microhardness of composites.

3.3 Mass transfer of electrodes

When the contact electrodes repeatedly open and close the circuit, erosion, and wear will occur. Meanwhile, some phenomena such as metal-liquid bridging arcing and spark discharge will occur. Metal transfer, splashing and vaporization, and mass loss and deformation occur on both sides of the electrode. It seriously affects the service life of the contact. However, the existing weigh test methods cannot accurately measure the erosion of composite; therefore, the mass transfer of contacts is often used to measure the severity of the material loss [56].

Figure 6 shows the mass change of Cu-Al_2O_3/30Mo/3SiC and 0.5Y_2O_3/Cu-Al_2O_3/30Mo/3SiC composites after 5,000 times switching operations under 25 V, DC and 10–30 A test conditions, respectively. It can be seen from Figure 6 that the mass of the two composites shows a trend of the mass increase of the anode and mass loss of the cathode, indicating the phenomenon of cathode material transfer to the anode. The mass of the cathode

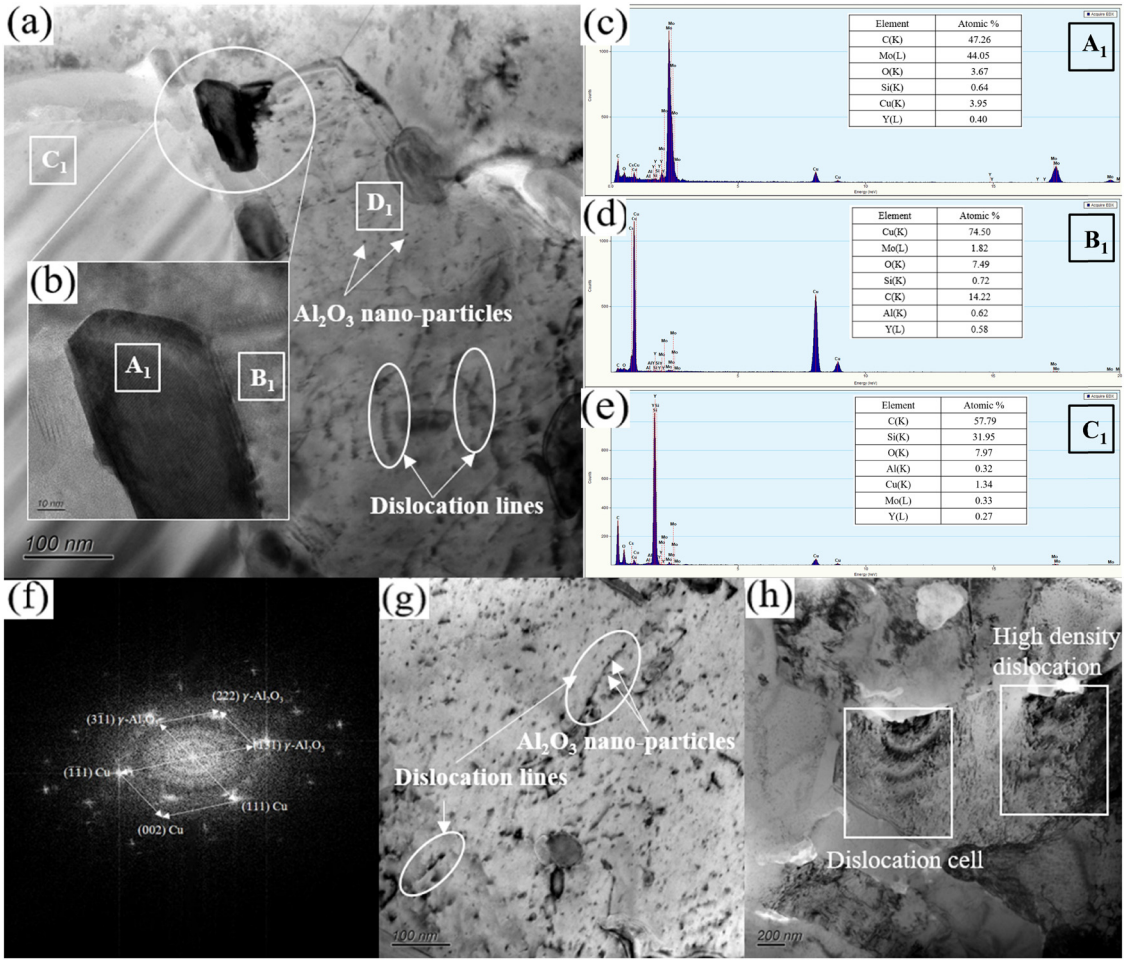

Figure 5: TEM and HRTEM images and EDS of the $0.5Y_2O_3$/Cu-Al_2O_3/30Mo/3SiC composite. (a, b, g, h) HRTEM images, (b) HRTEM image of the part area of (a), (c) EDS point of A_1 of (b), (d) EDS point of B_1 of (b), (e) EDS point of C_1 of (a), and (f) selected area electron diffraction pattern and indexing of alumina nano-particles of D_1 of (a).

and anode of composites gradually increase while the current increases from 10 to 30 A. The mass loss of the cathode and anode of the $0.5Y_2O_3$/Cu-Al_2O_3/30Mo/3SiC composite is generally lower than that of the Cu-Al_2O_3/30Mo/3SiC composite without the addition of nano-yttria, which shows that the addition of nano-yttria improves the arc erosion resistance of the composition. The density, electrical conductivity, and microhardness of the $0.5Y_2O_3$/Cu-Al_2O_3/30Mo/3SiC composite are improved to a certain extent after the addition of nano-yttria. The structure of the $0.5Y_2O_3$/Cu-Al_2O_3/30Mo/3SiC composite is more compact, which reduces the mass loss of the contact poles during the switching operations. The increase of electrical conductivity is beneficial to the current transmission of the composite contact material during the switching operation. The increase in the current transfer efficiency facilitates the improvement of the composite material's ability to resist arc erosion. It is found that the total mass

Table 3: Physical and mechanical properties of copper-based composites

Composites	Theoretical density/g cm^{-3}	True density/g cm^{-3}	Relative density/%	Electrical conductivity/ % IACS	Vickers hardness/HV
Cu-Al_2O_3/30Mo/3SiC	8.70	8.45	97.14	50.75	194
$0.5Y_2O_3$/Cu-Al_2O_3/ 30Mo/3SiC	8.67	8.54	98.46	51.59	206

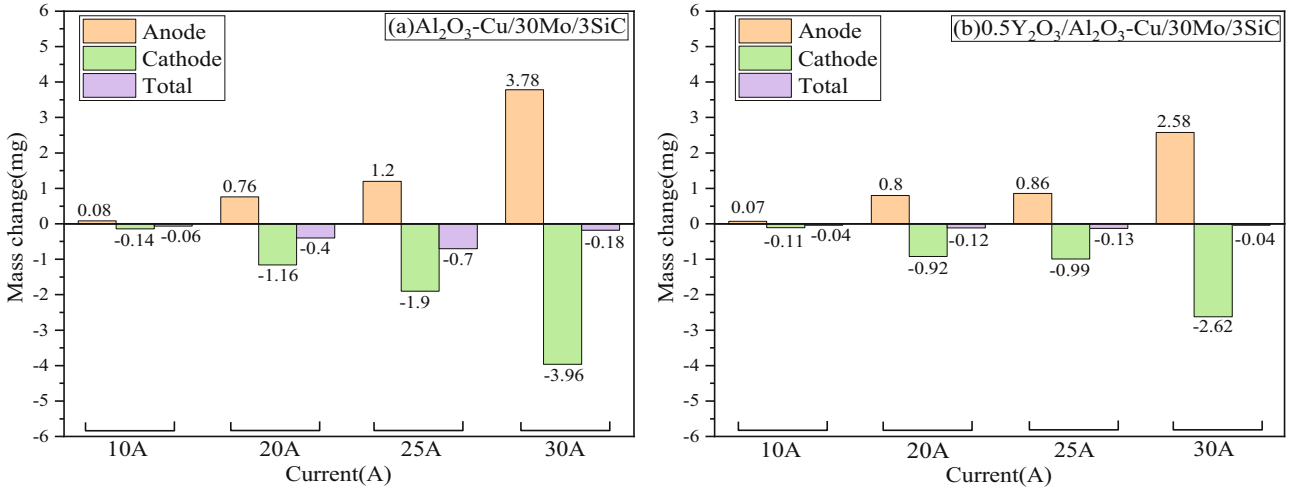

Figure 6: Mass change under 25 V, DC and 10–30 A test condition of composites. (a) Cu-Al_2O_3/30Mo/3SiC electrical contact and (b) 0.5Y_2O_3/Cu-Al_2O_3/30Mo/3SiC electrical contact.

change of the two composites is negative, indicating that a few materials are lost during the test. Interestingly, the mass loss of the composite was reduced by 77.8% when the current intensity reached 30 A. The mass loss of the composite material is mainly due to material migration or evaporation [57]. There is a less mass loss in this experiment compared to the work of Liang *et al.* [34]. This may be due to the formation of a high melting point molybdenum skeleton on the contact surface during arc erosion. These molybdenum skeletons are difficult to evaporate and vaporize.

3.4 Arc erosion morphology

Due to the arc heat flow input and arc force during the test of the contact material, the contact material will separate from the contact body in the form of evaporation, liquid splashing, or solid falling off. Arc erosion is the main form of contact material loss.

Figure 7 shows the erosion morphology of the contact surface of the composite after 5,000 switching operations under 25 V, DC and 30 A. Figure 7(a) and (b) shows the

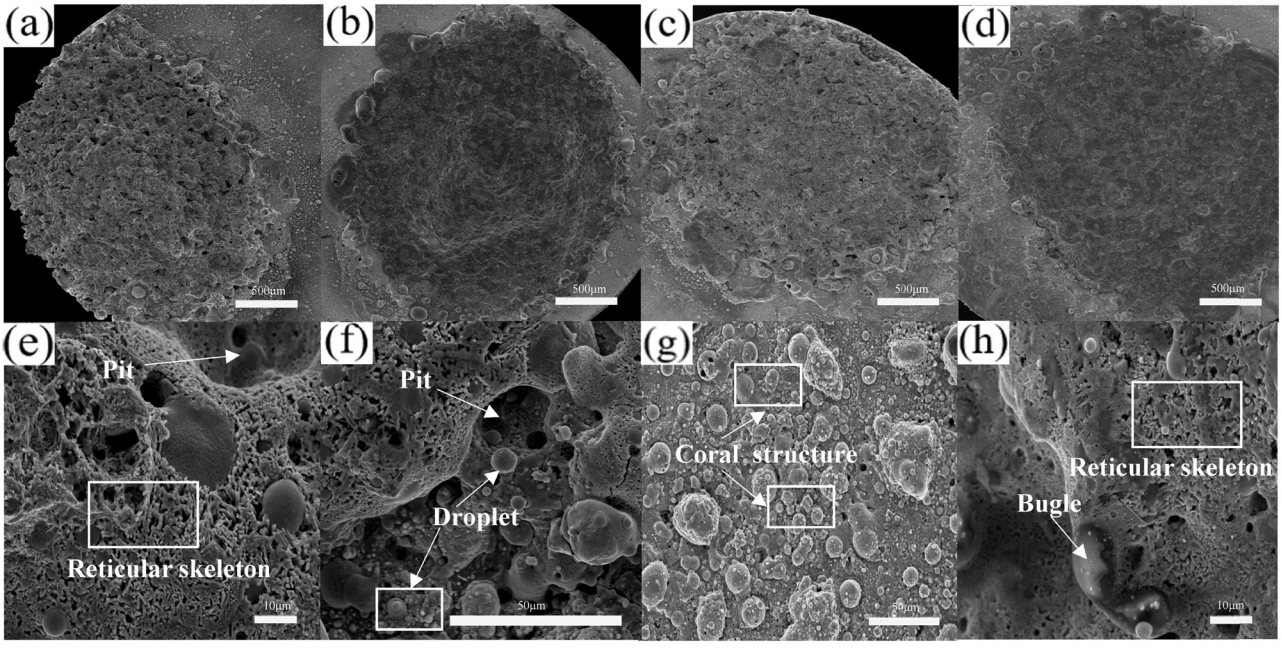

Figure 7: SEM images showing arc-eroded surface morphologies up to 5,000 switching operations at currents up to 30 A. (a, b, e, f) Cu-Al_2O_3/30Mo/3SiC and (c, d, g, h) 0.5Y_2O_3/Cu-Al_2O_3/30Mo/3SiC.

anode and cathode arc erosion morphology of the Cu-Al_2O_3/30Mo/3SiC composite, respectively, whereas Figure 7(c) and (d) shows that of the 0.5Y_2O_3/Cu-Al_2O_3/30Mo/3SiC composite, respectively. Figure 7(e)–(h) represents the partially enlarged view of the ablation morphology of the two composites, showing typical arc erosion morphology such as the reticular skeleton, droplet, bulge, pore, paste peak, and coral structure.

Figure 8 shows the 3-D arc erosion surface morphology of the composite after 5,000 switching operations at 25 V, DC and 30 A. The scanning range is 1,600 mm × 1,600 mm. Figure 8(a) and (b) shows the 3-D morphology of the anode and cathode of the Cu-Al_2O_3/30Mo/3SiC composite, respectively, whereas Figure 8(c) and (d) show that of the 0.5Y_2O_3/Cu-Al_2O_3/30Mo/3SiC composite, respectively. It can be seen from the diagram that after 5,000 switching operations, the anode surface is convex and the cathode surface is concave. There were many mountain-like protrusions on the anode surface and many canyon-like pits on the cathode surface, indicating that the material on the electrode surface migrated from the cathode to the anode.

In order to explore the element distribution on the electrode surface after arc erosion, the element distribution on the electrode surface is further analyzed by EDS, as shown in Figure 9. The droplet-like material is mainly composed of copper. Copper has a low melting point and could be spattered in the form of droplets during electrical contact. The droplets rapidly cool in the air to form copper balls. Molybdenum has a relatively high melting point. It realizes rapid solidification in an argon environment after melting, which mainly forms the network skeleton in the eroded surface morphology. At the same time, in addition to the copper base, the nano-yttria, alumina, and silicon carbide are also redistributed on the skeleton, which indicates that in the process of the electrical contact, the surface achieves a redistribution of elements.

3.5 Arc duration and energy

The main form of arc erosion is the evaporation and splashing of the contact material due to local overheating under the action of the arc, resulting in material loss. Arc erosion is the most important factor affecting the contact life of the switchgear [58]. Therefore, it is necessary to discuss the arc duration and arc energy during arc erosion.

The arc current, contact material, contact surface condition, and contact separation speed will affect the arcing duration [59,60]. This work focuses on the variation of arc duration for different contact materials after 5,000 contact tests at 25 V, DC and 30 A. Figure 10(a) and (b) shows the variation rule of arc duration and arc energy with contact times. The arcing duration of the Cu-Al_2O_3/30Mo/3SiC composite shows an upward trend at about 1,300 times, a downward trend at about 1,700 times, and then it is in a stable state. While the 0.5Y_2O_3/Cu-Al_2O_3/30Mo/3SiC composite shows an upward trend at about 700 times and a

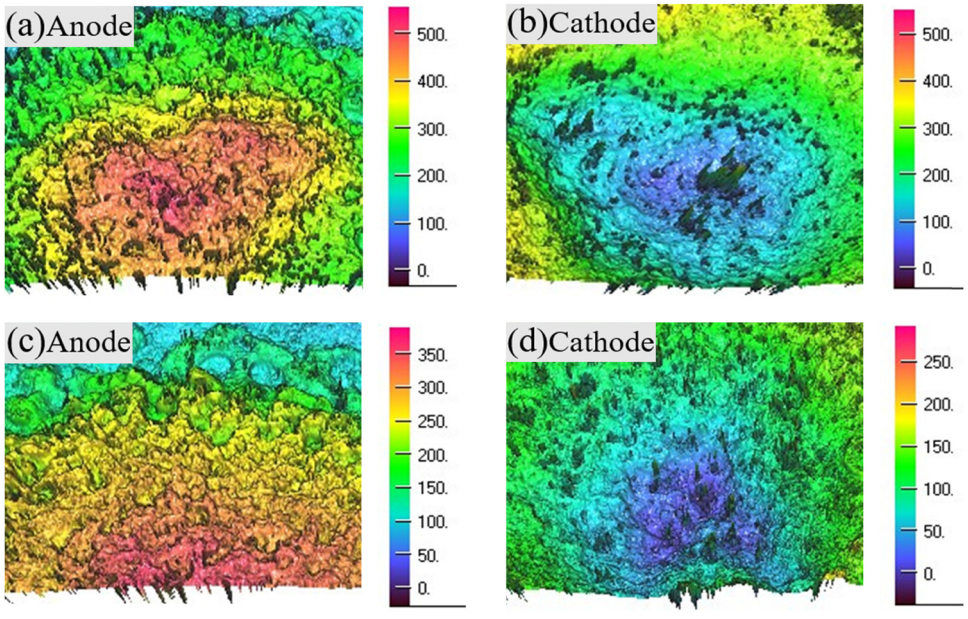

Figure 8: 3-D surface morphology of composites operating at 25 V, DC and 30 A. (a and b) Cu-Al_2O_3/30Mo/3SiC and (c and d) 0.5Y_2O_3/Cu-Al_2O_3/30Mo/3SiC.

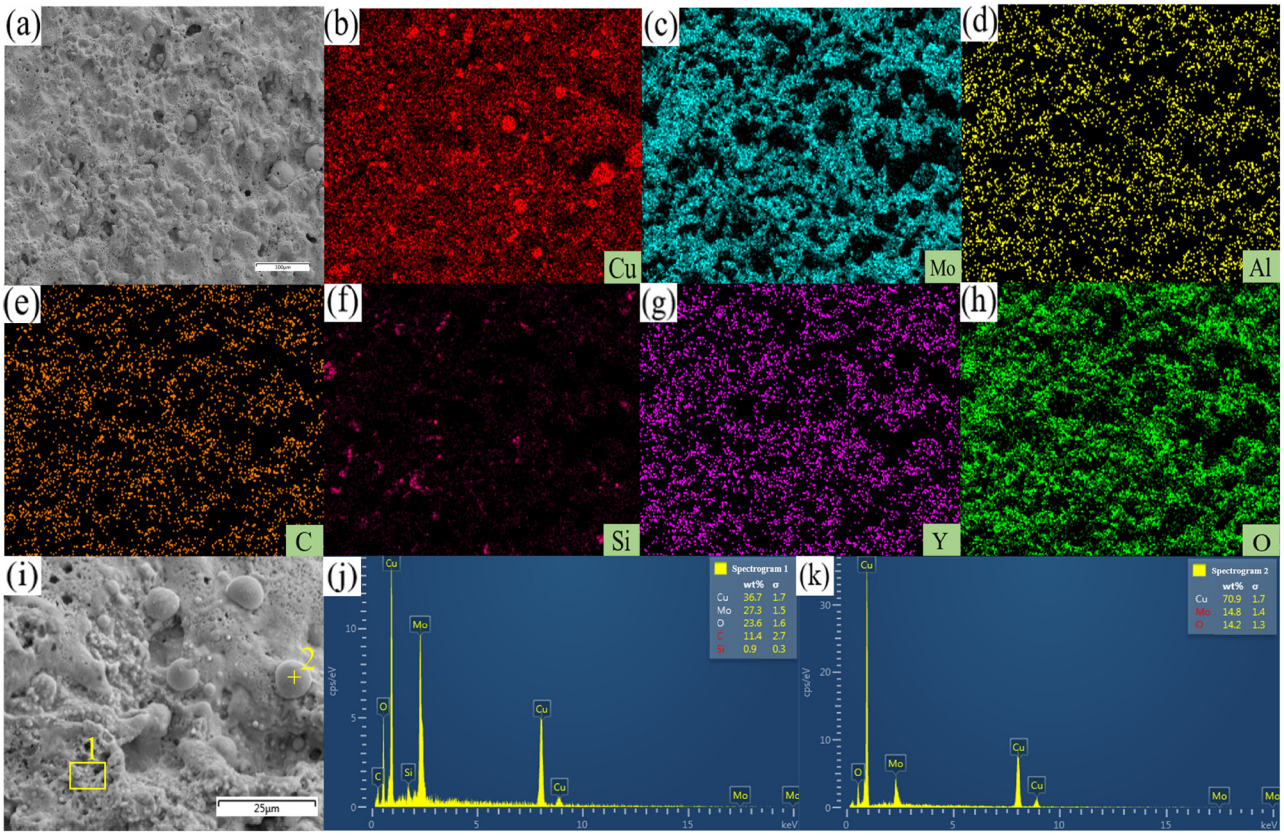

Figure 9: EDS element maps after the electric contact experiment of the $0.5Y_2O_3$/Cu-Al_2O_3/30Mo/3SiC composite operation at 25 V, DC and 30 A. (a, i) BSE images, (b) Cu Kα1, (c) Mo Lα1, (d) Al Kα1, (e) C Kα1-2, (f) Si Kα1, (g) Y Lα1, (h) O Kα1, (j) dot scan of point one of (i), and (k) dot scan of point two of (i).

downward trend at about 1,000 times, and then shows a steady state. With the increase of contact times, the arc burning time of the $0.5Y_2O_3$/Cu-Al_2O_3/30Mo/3SiC composite is shorter and more stable than that of the Cu-Al_2O_3/30Mo/3SiC composite. Comparing Figure 10(a) and (b), it can be seen that the arc duration and arc energy of the contact material show a similar change trend, indicating that the arc duration and arc energy may show a certain linear relationship. Therefore, the scatter diagram of the corresponding relationship between arcing duration and arcing energy of the two composites was plotted, and the fitting equations were established. Figure 10(c) and (d) shows the fitting curve of arcing duration and arcing energy of the two composites. It can be seen that there is a certain linear relationship between arcing duration and arcing energy of the two composites. After fitting the data, the results are as follows:

$$E_1 = 75.74t - 11.42 \quad R^2 = 0.99, \tag{2}$$

$$E_2 = 67.41t - 6.71 \quad R^2 = 0.99. \tag{3}$$

Equation (2) is the fitting equation of the Cu-Al_2O_3/30Mo/3SiC composite, and equation (3) is that of the $0.5Y_2O_3$/Cu-Al_2O_3/30Mo/3SiC composite. It can be seen from the above equations that under the condition of 25 V, DC and 30 A, when the arc duration is greater than 0.57 ms, the $0.5Y_2O_3$/Cu-Al_2O_3/30Mo/3SiC composite has a shorter average arc duration than the Cu-Al_2O_3/30Mo/3SiC composite. This is consistent with the results of Zhang *et al.* [17]. However, the arc burning energy decreased with a short arc duration due to the addition of nano-yttria in this experiment. This is mainly because nano-yttria has a high melting point and good chemical stability. At the same time, owing to the good high-temperature stability of nano-yttria, it stably exists in the copper base in the process of powder metallurgy [61], which prevents the abnormal growth of grains, and effectively improves the arc erosion resistance of the composite. Therefore, the $0.5Y_2O_3$/Cu-Al_2O_3/30Mo/3SiC composite has better arc extinguishing ability.

3.6 Arc erosion rates

The form of arc erosion generally varies with different materials and current conditions [62]. The electrode surface of

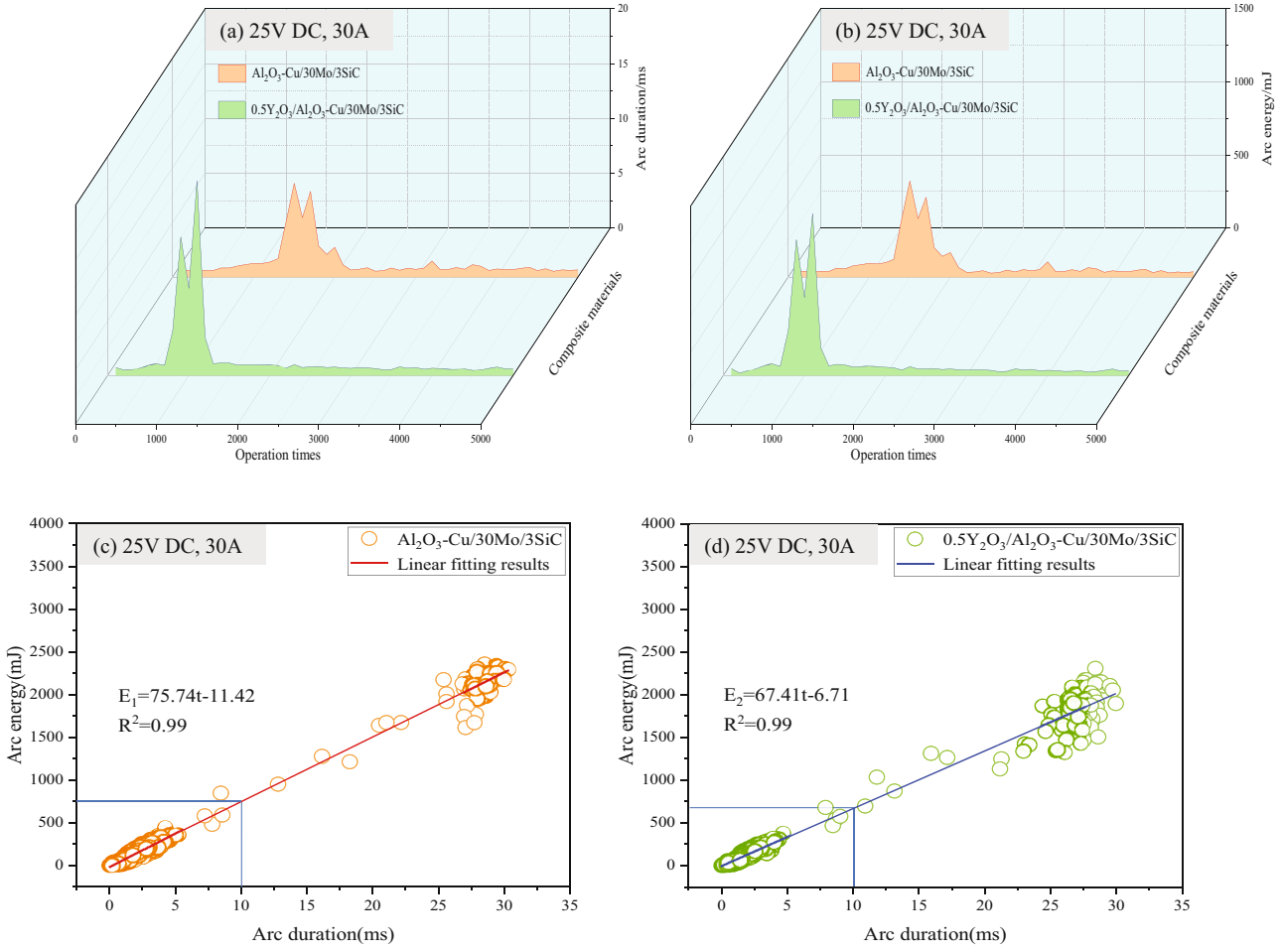

Figure 10: Relationship of the arc energy, the arc duration, and operation times of the two composites at 25 V, DC and 30 A. (a) Variation of arc duration of Cu-Al_2O_3/30Mo/3SiC and 0.5Y_2O_3/Cu-Al_2O_3/30Mo/3SiC composites with operation times, (b) variation of arc energy of the two composites with operation times, (c) relationship between arc duration and arcing energy of the Cu-Al_2O_3/30Mo/3SiC composite, and (d) relationship between arc duration and arc energy of the 0.5Y_2O_3/Cu-Al_2O_3/30Mo/3SiC composite.

the contact material mainly vaporizes when the current passing through the test is small. When the current increases, not only the gasification and evaporation of the material but also the splashing of liquid metals occurs. The strong droplet splashing will become the main form of contact material erosion when the current is further increased. Therefore, a large number of droplets appear on the electrode surface at 25 V, DC and 30 A in this work, as shown in Figure 7. The arc erosion rate is an important parameter in characterizing the arc erosion of the contact material, *i.e.*, the ratio of the material weight or volume loss to some characteristic value. Generally, the amount of material erosion per unit of arc energy φ is used as the erosion rate:

$$\varphi = \Delta m / W, \tag{4}$$

where Δm represents the mass change before and after erosion and W represents the arc energy.

At 25 V, DC and 30 A, 5,000 switching operations were carried out on the two composites, and their mass loss and arc energy change were discussed as examples:

$$\varphi_1 = \Delta m_1 / W_1 = 4.95 \times 10^{-7} \text{g/J}, \tag{5}$$

$$\varphi_2 = \Delta m_2 / W_2 = 1.01 \times 10^{-7} \text{g/J}, \tag{6}$$

where φ_1, Δm_1, and W_1 represent the erosion rate, the mass change before and after erosion, and the total arc energy, respectively, of the Cu-Al_2O_3/30Mo/3SiC composite. φ_2, Δm_2, and W_2 are the erosion rate composite, the mass change before and after erosion, and the total arc energy, respectively, of 0.5Y_2O_3/Cu-Al_2O_3/30Mo/3SiC. At 25 V, DC and 30 A, the arc erosion rate of the composites decreased by 10.45% after the addition of nano-yttria. It also shows that the arc erosion resistance of the Cu-Al_2O_3/30Mo/3SiC composite improves to a great extent by the addition of a small amount of nano-yttria.

3.7 Welding force

In the process of the electrical contact test, the electrical contacts of the cathode and anode are continuously and repeatedly opened and closed. A contact force of 40–60 cN is applied between the cathode and anode in this work. Liquid metal bridging and melting to a certain extent will occur between the contacts under this contact force. It is the welding process of the contact material. The welding force is the force required to separate two fused contacts. However, welding of the contact material will seriously damage the service life of contacts, so it is necessary to reduce the welding force to improve the service life of the contact material. To improve the comprehensive performance of contacts, the most effective measure is to increase the anti-fusion weldability of contacts besides improving the breaking operation force of contacts. The main ways include improving the electrical conductivity and heat transfer characteristics of the contact, increasing the melting point and hot melting, and reducing the fusion welding force of the contact material.

Figure 11 shows the relationship between the welding force of Cu-Al_2O_3/30Mo/3SiC and 0.5Y_2O_3/Cu-Al_2O_3/30Mo/3SiC composites and the operation times of contact disconnections during the electrical contact test at 25 V, DC and 10 A and 25 V, DC and 30 A, respectively. Each data point represents the average value of 100 cycles. It can be seen from Figure 11 that the welding force tends to stabilize as the number of operations increases. Assuming that the tensile strength at the welding position is equal to that of the contact material, the welding force depends on the current-carrying contact area and the tensile strength of the contact material:

$$F = \sigma S, \tag{7}$$

where F is the welding force, σ is the tensile strength, and S is the current-carrying contact surface area.

It can be seen from Figure 11 that the welding force of the 0.5Y_2O_3/Cu-Al_2O_3/30Mo/3SiC composite is generally lower than that of the Cu-Al_2O_3/30Mo/3SiC composite. The calculation result shows that the average welding force of the Cu-Al_2O_3/30Mo/3SiC composite is about 38.06 cN, and that of the 0.5Y_2O_3/Cu-Al_2O_3/30Mo/3SiC composite is about 34.40 cN at 25 V, DC and 10 A. The average welding force of the Cu-Al_2O_3/30Mo/3SiC composite is about 38.20 cN and that of the 0.5Y_2O_3/Cu-Al_2O_3/30Mo/3SiC composite is about 36.76 cN at 25 V, DC and 30 A. It can be found that the average welding force of the 0.5Y_2O_3/Cu-Al_2O_3/30Mo/3SiC composite is slightly lower than that of the Cu-Al_2O_3/30Mo/3SiC composite. This shows that the addition of nano-yttria can reduce the welding force and improve the welding resistance of the Cu-Al_2O_3/30Mo/3SiC composite. The main reason is that the conductivity, density, and microhardness of the 0.5Y_2O_3/Cu-Al_2O_3/30Mo/3SiC composite are better after the addition of nano-yttria. These improvements synergistically acted on the fusion welding resistance of the Cu-Al_2O_3/30Mo/3SiC composite. Simultaneously, the affinity of nano-yttria particles to Cu is small. Nano-yttria particles were dispersed in the 0.5Y_2O_3/Cu-Al_2O_3/30Mo/3SiC composite, which reduced the fluidity of copper in the composites. It is difficult to splash copper droplets during an electrical contact. Also, it is difficult for

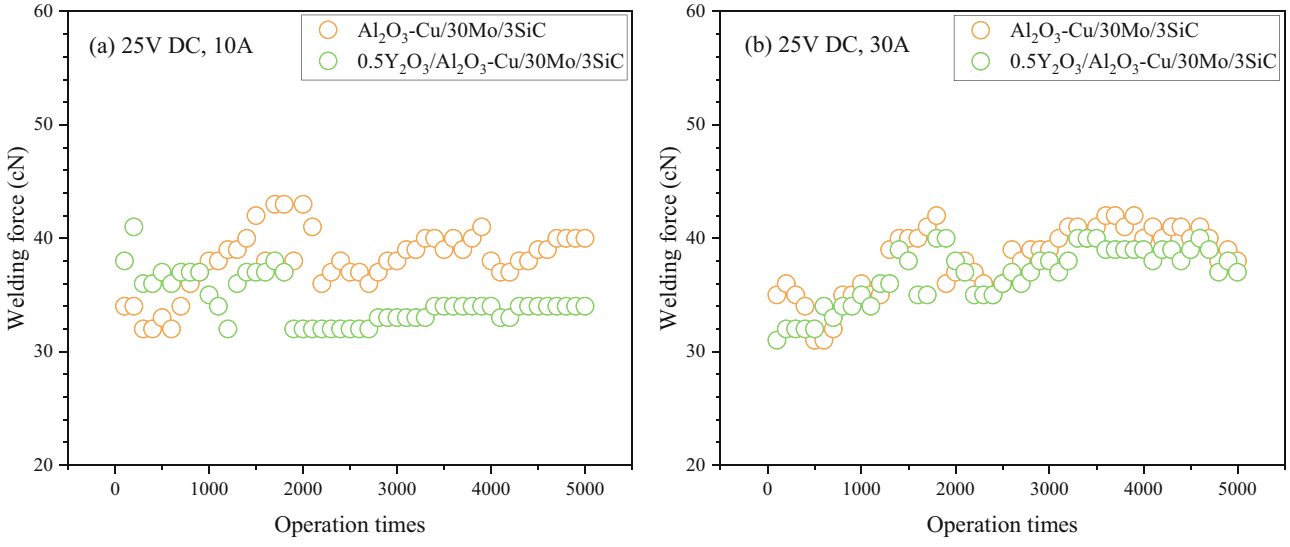

Figure 11: Relationship between the welding force and operation times of Cu-Al_2O_3/30Mo/3SiC and 0.5Y_2O_3/Cu-Al_2O_3/30Mo/3SiC composites: (a) 25 V, DC and 10 A and (b) 25 V, DC and 30 A.

the welding process to proceed smoothly when the droplets are not splashed, which reduced the welding force. The results of Mu *et al.* [42] also showed that the addition of yttria can reduce the welding force of the material.

4 Conclusion

1) The Cu-Al_2O_3/30Mo/3SiC and 0.5Y_2O_3/Cu-Al_2O_3/30Mo/3SiC composites were prepared by fast-hot-pressing sintering technology combined with the internal oxidation method. TEM analysis indicates that the alumina nanoparticles disperse on the copper base.
2) The relative density of the composite reaches more than 98%, and the microhardness reaches 208 HV after the addition of nano-yttria nanoparticles. This is mainly due to the dispersion distribution of nano-yttria nanoparticles and alumina nano precipitate during sintering and the internal oxidation process.
3) Under the experimental conditions of 25 V, DC and 10–30 A, the mass of the cathode decreases, the mass of the anode increases, and the total mass change increases. The addition of nano-yttria improves the mechanical and physical properties of composites. These improved properties reduce the loss of the material during the electrical contact and decrease the fusion force of the composite.
4) By characterizing the element distribution on the electrode surface before and after the electrical contact test, it can be found that the element distribution on the electrode surface changes significantly before and after the electrical contact, which shows that the element redistribution occurs during the process of the electrical contact.

Funding information: This work was supported by the National Natural Science Foundation of China (52071134), the Program for Innovative Research Team at the University of Henan Province (22IRTSTHN001), China Postdoctoral Science Foundation (2020M682316, 2021T140779), Scientific Research and Development Special Project of Henan Academy of Sciences (220910009), and Key R & D and promotion projects in Henan Province (212102210117).

Author contributions: All authors have accepted responsibility for the entire content of this manuscript and approved its submission.

Conflict of interest: The authors state no conflict of interest.

References

[1] Qi JJ, Gao X, Huang NT. Mechanical fault diagnosis of a high voltage circuit breaker based on high-efficiency time-domain feature extraction with entropy features. Entropy. 2020;22(4):478–93.
[2] Hu W, Westerlund P, Hilber P, Chen C, Yang Z. A general model, estimation, and procedure for modeling recurrent failure process of high-voltage circuit breakers considering multivariate impacts. Reliab Eng Syst Safe. 2022;220:108276.
[3] Di L, Xiao Y, Hu F, Liang Y, Tan J, You Y. Real-time monitoring of high voltage switch based on CAD. Adv Multimed. 2022;2022:1–9.
[4] Lech M, Wgierek P, Kozak C, Pastuszak J. Methodology for testing the electric strength of vacuum chambers designed for modern medium voltage switchgear. Metrol Meas Syst. 2021;27(4):687–700.
[5] Liang S, Zhou M, Zhang Y, Liu S, Li X, Tian B, et al. Thermal deformation behavior of GO/CeO_2 in-situ reinforced Cu30Cr10W electrical contact material. J Alloy Compd. 2022;899:163266.
[6] Nachiketa R, Bernd K, Timo M, Ludo F, Kim V, Jef V. Effect of WC particle size and Ag volume fraction on electrical contact resistance and thermal conductivity of Ag-WC contact materials. Mate Des. 2015;85:412–22.
[7] Chen WG, Chen MZ, Xing LQ, Li JS, Hong F. Effect of doping on electrical arc characteristic of WCu electrical contact materials. Chin J Nonferrous Met. 2009;19(11):2029–3037.
[8] Guo XH, Song KX, Liang SH, Zhou YJ, Wang X. Relationship between the MgO_p/Cu interfacial bonding state and the arc erosion resistance of MgO/Cu composites. J Mater Res. 2017;32(19):3753–60.
[9] Grechanyuk NI, Konoval VP, Grechanyuk VG, Bagliuk GA, Myroniuk DV. Properties of Cu–Mo materials produced by physical vapor deposition for electrical contacts. Powder Metall Met Ceram. 2021;60(3-4):183–90.
[10] Li HY, Wang XH, Hu ZD, Liu YF. Investigation of arc erosion mechanism for tin dioxide-reinforced silver-based electrical contact material under direct current. J Electron Mater. 2020;49:4730–40.
[11] Li H, Wang X, Liang Y, Fei Y, Zhang H. Effect of electrical contact mode on the arc-erosion behavior of titanium diboride-nickel co-reinforced and nickel-enhanced silver-based electrical contact materials. J Electron Mater. 2022;51:1–11.
[12] Li HY, Wang XH, Liu YF, Guo XH. Effect of strengthening phase on material transfer behavior of Ag-based contact materials under different voltages. Vacuum. 2017;135:55–65.
[13] Li L, Liu S, Zhou M, Zhang Y, Liang S, Huang J, et al. Microstructure evolution of graphene reinforced Cu/CeO_2/Cr electrical contact materials under thermal deformation behavior. J Mater Res Technol. 2022;18:1412–23.
[14] Wang XH, Yang H, Chen M, Zou JT, Liang SH. Fabrication and arc erosion behaviors of $AgTiB_2$ contact materials. Powder Technol. 2014;256:20–4.
[15] Wang J, Kang Y, Wang C. Microstructure and vacuum arc characteristics of CuO skeletal structure Ag-CuO contact materials. J Alloy Compd. 2016;686:702–7.
[16] Zhang P, Ngai TL, Wang AD, Ye ZY. Arc erosion behavior of Cu-Ti_3SiC_2 cathode and anode. Vacuum. 2017;141:235–42.

[17] Zhang X, Zhang Y, Tian B, An J, Zhao Z, Volinsky AA, et al. Arc erosion behavior of the Al_2O_3-Cu/(W, Cr) electrical contacts. Compos Part B-Eng. 2019;160:110–8.
[18] Zhang C, Qiao S, Yang Z, Ding B. Cathode spot movements along the carbon fibers in carbon/carbon composites. J Phys D Appl Phys. 2007;40(13):3980–4.
[19] Gorbatyuk S, Pashkov A, Chichenev N. Improved copper-molybdenum composite material production technology. Mater Today Proc. 2019;11:31–5.
[20] Biyik S. Characterization of nanocrystalline Cu25Mo electrical contact material synthesized via ball milling. Acta Phys Pol A. 2017;132(3):886–8.
[21] Lin HR, Guo XH, Song KX, Feng J, Li SL, Zhang XF. Synergistic strengthening mechanism of copper matrix composite reinforced with nano-Al_2O_3 particles and micro-SiC whiskers. Nanotechnol Rev. 2021;10(1):62–72.
[22] Wang XL, Wang YP, Su Y, Qu ZG. Synergetic strengthening effects on copper matrix induced by Al_2O_3 particle revealed from micro-scale mechanical deformation and microstructure evolutions. Ceram Int. 2019;45(12):14889–95.
[23] Hussain MZ, Khan U, Jangid R, Khan S. Hardness and wear analysis of Cu/Al_2O_3 composite for application in EDM electrode. IOP Conf Ser Mater Sci Eng. 2018;310(1):012044.
[24] Wagih A, Abu-Oqail A, Fathy A. Effect of GNPs content on thermal and mechanical properties of a novel hybrid Cu-Al_2O_3/GNPs coated Ag nanocomposite. Ceram Int. 2019;45(1):1115–24.
[25] Akbarpour MR, Salahi E, Hesari FA, Kim HS, Simchi A. Effect of nanoparticle content on the microstructural and mechanical properties of nano-SiC dispersed bulk ultrafine-grained Cu matrix composites. Mater Des. 2013;52:881–7.
[26] Dong RH, Yang WS, Wu P, Murid H, Wu GH, Jiang LT. High content SiC nanowires reinforced Al composite with high strength and plasticity. Mater Sci Eng. 2015;630:8–12.
[27] Feng J, Song KX, Liang SH, Guo XH, Li SL. Mechanical properties and electrical conductivity of oriented-SiC-whisker-reinforced Al_2O_3/Cu composites. J Mater Res Technol. 2022;20:1470–80.
[28] Biyik S, Arslan F, Aydin M. Arc-erosion behavior of boric oxide-reinforced silver-based electrical contact materials produced by mechanical alloying. J Electron Mater. 2015;44(1):457–66.
[29] Yang X, Liang S, Wang X, Xiao P, Fan Z. Effect of WC and CeO_2 on microstructure and properties of W-Cu electrical contact material. Int J Refract Met Hard Mater. 2010;28(2):305–11.
[30] Yang R, Liu S, Cui H, Yang H, Zeng Y, Liu M, et al. Quasi-continuous network structure greatly improved the anti-arc-erosion capability of Ag/Y_2O_3 electrical contacts. Mater. 2022;15(7):2450.
[31] Kang W, Ozgur DO, Varma A. Solution combustion synthesis of high surface area CeO_2 nanopowders for catalytic applications: reaction mechanism and properties. ACS Appl Nano Mater. 2018;1(2):675–85.
[32] Elayakumar K, Dinesh A, Manikandan A, Palanivelu M, Kavitha G, Prakash S, et al. Structural, morphological, enhanced magnetic properties and antibacterial bio-medical activity of rare earth element (REE) cerium (Ce^{3+}) doped $CoFe_2O_4$ nanoparticles. J Magn Magn Mater. 2019;476:157–65.
[33] Liu S, Li L, Zhou M, Liang S, Zhang Y, Huang J, et al. Preparation and properties of graphene reinforced Cu/0.5$CeO_2$30Cr electrical contact materials. Vacuum. 2022;195:110687.
[34] Liang S, Liu S, Zhang Y, Zhou M, Tian B, Geng Y, et al. Effect of in situ graphene-doped nano-CeO_2 on microstructure and electrical contact properties of Cu30Cr10W contacts. Nanotechnol Rev. 2021;10(1):385–400.
[35] Baulin O, Douillard T, Fabrègue D, Perez M, Pelletier JM, Bugnet M. Three-dimensional structure and formation mechanisms of Y_2O_3 hollow-precipitates in a Cu-based metallic glass. Mater Des. 2019;168:107660.
[36] Liu T, Shen HL, Wang CX, Chou WS. Structure evolution of Y_2O_3 nanoparticle/Fe composite during mechanical milling and annealing. Prog Nat Sci Mater Int. 2013;2(4):434–9.
[37] Yang XH, Fan ZK, Liang SH, Xiao P. Effects of Y_2O_3 on properties of Cu-W electrical contact materials. Chin J Mater Res. 2007;21:415–9.
[38] Nagorka MS, Levi CG, Lucas GE, Ridder SD. The potential of rapid solidification in oxide-dispersion-strengthened copper alloy development. Mater Sci Eng A. 1991;142:277–89.
[39] Groza JR, Gibeling JC. Principles of particle selection for dispersion-strengthened copper. Mater Sci Eng A. 1993;171:115–25.
[40] Huang F, Wang H, Yang B, Liao T, Wang Z. Uniformly dispersed Y_2O_3 nanoparticles in nanocrystalline copper matrix via multi-step ball milling and reduction process. Mater Lett. 2019;242:119–22.
[41] Huang B, Hishinuma Y, Noto H, Kasada R, Oono N, Ukai S, et al. In-situ fabrication of yttria dispersed copper alloys through MA-HIP process. Nucl Mater Energy. 2018;16:167–74.
[42] Mu Z, Geng HR, Li MM, Nie GL, Leng JF. Effects of Y_2O_3 on the property of copper-based contact materials. Compos Part B-Eng. 2013;52:51–5.
[43] Biyik S, Aydin M. Fabrication and arc-erosion behavior of Ag8SnO_2 electrical contact materials under inductive loads. Acta Phys Polonica A. 2017;131(3):339–42.
[44] Pillari LK, Bakshi SR, Chaudhuri P, Murty BS. Fabrication of W-Cu functionally graded composites using high energy ball milling and spark plasma sintering for plasma facing components. Adv Powder Technol. 2020;220:108276–3666.
[45] Mozammil S, Karloopia J, Verma R, Jha PK. Mechanical response of friction stir butt weld Al-4.5%Cu/TiB_2/2.5p in situ composite: Statistical modelling and optimization. J Alloy Compd. 2020;826:154184.
[46] Zhou X, Yi D, Nyborg L, Hu Z, Huang J, Cao Y. Influence of Ag addition on the microstructure and properties of copper-alumina composites prepared by internal oxidation. J Alloy Compd. 2017;722:962–9.
[47] Huang W, Shishehbor M, Guarín-Zapata N, Kirchhofer ND, Li J, Cruz L, et al. A natural impact-resistant bicontinuous composite nanoparticle coating. Nat Mater. 2020;19(11):1236–43.
[48] Biyik S. Influence of type of process control agent on the synthesis of Ag8ZnO composite powder. Acta Phys Pol A. 2019;135(4):778–81.
[49] Akbarpour MR, Mirabad HM, Alipour S. Microstructural and mechanical characteristics of hybrid SiC/Cu composites with nano-and micro-sized SiC particles. Ceram Int. 2019;45(3):3276–83.
[50] Câmara NT, Raimundo RA, Lourenço CS, Morais LMF, Silva DDS, Gomes RM, et al. Impact of the SiC addition on the morphological, structural and mechanical properties of Cu-SiC composite powders prepared by high energy milling. Adv Powder Technol. 2021;32(8):2950–61.

[51] Ding H, Chu W, Liu Q, Wang H, Hao C, Jia H, et al. Microstructure evolution of Cu-TiC composites with the change of Ti/C ratio. Results Phys. 2019;14:102369.
[52] Biyik S. Effect of cubic and hexagonal boron nitride additions on the synthesis of Ag-SnO_2 electrical contact material. J Nanoelectron Optoe. 2019;14(7):1010–5.
[53] Zhuo H, Tang J, Ye N. A novel approach for strengthening Cu-Y_2O_3 composites by in situ reaction at liquidus temperature. Mat Sci Eng A. 2013;584:1–6.
[54] Qin YQ, Tian Y, Zhuang Y, Luo LM, Zan X, Wu YC. Effects of solid-liquid doping and spark plasma sintering on the microstructure and mechanical properties of the alloy Y_2O_3-doped copper matrix composites. Vacuum. 2021;192:110436.
[55] Feng J, Song K, Liang S, Guo X, Jiang Y. Electrical wear of TiB_2 particle-reinforced Cu and Cu-Cr composites prepared by vacuum arc melting. Vacuum. 2020;175:109295.
[56] Guo X, Yang Y, Song K, Shaolin L, Jiang F, Wang X. Arc erosion resistance of hybrid copper matrix composites reinforced with CNTs and micro-TiB_2 particles. J Mater Res Technol. 2021;11:1469–79.
[57] Biyik S, Aydin M. Investigation of the effect of different current loads on the arc-erosion performance of electrical contacts. Acta Phys Pol A. 2016;129(4):656–60.
[58] Zhu S, Liu Y, Tian B, Zhang Y, Song K. Arc erosion behavior and mechanism of Cu/Cr_2O electrical contact material. Vacuum. 2017;143:129–37.
[59] Niwa Y, Funahashi T, Yokokura K, Matsuzaki J, Homma M, Kaneko E. Basic investigation of a high-speed vacuum circuit breaker and its vacuum arc characteristics. IEE Proc Gener Transm Distrib. 2006;153:11–5.
[60] Li H, Wang X, Liu J, Zhang H, Fei Y. Effect of electric load characteristics on the arc-erosion behavior of Ag-4 wt%TiB_2-4 wt%Ni electrical contact material. Appl Phys A-Mater. 2021;326:112718.
[61] Zhang D, Qin M, Huang M, Wu T, Jia B, Wu H, et al. Magnetic properties of evenly mixed Fe-Y_2O_3 nanocomposites synthesized by a facile wet-chemical based route. J Magn Magn Mater. 2019;491:165576.
[62] Wang J, Kang Y, Wang C, Wang J, Fu C. Resistance to arc erosion characteristics of CuO skeleton-reinforced Ag-CuO contact materials. J Alloy Compd. 2018;756:202–7.